PAPER

Check for updates

Morphology of vesicle triplets: shape transformation at weak and strong adhesion limits†

Toshikaze Chiba, [a] Yuka Sakuma, [a] Masayuki Imai *[a] and Primož Ziherl [bc]

We investigate the morphologies of adhering vesicle triplets as a function of volume-to-area ratio encoded by the reduced volume in strong and weak adhesion regimes. In the strong adhesion regime, the morphology change of the vesicle triplet depends on the arrangement of vesicles. By decreasing the reduced volume, a triangular triplet composed of three spherical caps with a trifurcated flat contact zone deformed to a compact spherical shape with a sigmoidal contact zone, whereas a linear vesicle triplet composed of pancake-shaped vesicles sandwiched between two spherical-cap vesicles with a flat contact zone deformed into a compact spherical shape with biconvex interfaces. The morphologies of vesicle triplets with flat contact zones are reproduced by the so-called two-tension model based on the total energy consisting of bending energy, adhesion energy and surface energy, where the surface tension in the noncontact zone is different from that in the contact zone. When the flat interface deforms, the two-tension model is no longer applicable. The compact spherical triplets with curved interfaces can be reproduced by introducing geometrical constraints requiring that the total area of the non-contact zones is minimal, thereby confining the aggregate to a spherical cavity; this is referred to as the cavity model. In the weak adhesion regime, vesicle triplets with either a triangular or linear topology deform into prolate-based triplets by decreasing the reduced volume.

1 Introduction

Cellular structures separated by closed membranes are frequently found around us. For example, a soap bubble is a spherical cellular structure partitioned by a thin water layer sandwiched between surfactant monolayers in the air. When a few soap bubbles meet, two adjacent layers at the contact zone merge, and they form characteristic multicellular patterns consisting of spherical caps and contact zones so as to minimize the surface energy, where the mean curvature is the same in each point of a given contact zone.[1] The contact zones meet in threes at an angle of 120° to form an edge known as the Plateau border. The Plateau borders meet in fours at the tetrahedral angle so as to form a vertex. These geometrical laws governing soap bubble aggregates are called Plateau rules.[2]

In contrast to a soap bubble, a vesicle—a closed surfactant bilayer suspended in water—shows a variety of shapes that minimize the bilayer bending energy at a given volume and area.[3,4] A typical example of a vesicular structure is a mammalian red blood cell (RBC) which has a disklike biconcave shape with the reduced volume $v \approx 0.60$ ($v = 6\pi^{1/2}V/A^{3/2}$, where A and V are the membrane area and the enclosed volume, respectively).[5,6] The disklike biconcave shape agrees well with the prediction of the bending energy model.[7,8] When a few RBCs form an aggregate, the contact zone shows a flat, concave, or sigmodal shape[9,10] even in microcapillary flow.[11–13] The static shape depends on the balance between the membrane bending energy and adhesion energy at the fixed reduced volume and adhesion strength.[14–16] However, the morphology of RBC aggregates is strongly restricted by the constant reduced volume constraint. To release the constraint, we investigated the morphology of vesicle aggregates as a function of the reduced volume. For example, we studied the morphology of a vesicle doublet.[17] As the reduced volume is decreased in the strong adhesion regime, the vesicle doublet with spherical caps and a flat contact zone deforms into a compact spherical doublet with the sigmoidal contact zone, whereas in the weak adhesion regime the vesicle doublet with spherical caps and a flat contact zone deforms into a parallel prolate doublet. Thus, our vesicle aggregates can present multicellular patterns which are not seen in aggregates of soap bubbles.

[a] Department of Physics, Tohoku University, Aoba, Sendai, 980-8578, Japan. E-mail: imai@bio.phys.tohoku.ac.jp

[b] Faculty of Mathematics and Physics, University of Ljubljana, Jadranska 19, SI-1000 Ljubljana, Slovenia

[c] Jožef Stefan Institute, Jamova 39, SI-1000 Ljubljana, Slovenia

† Electronic supplementary information (ESI) available. See DOI: https://doi.org/10.1039/d3sm00308f

Morphological changes due to vesicle adhesion have been studied in many systems, such as vesicles adhering to other vesicles,[17–19] substrates,[20,21] and colloidal particles.[22–26] In this study, we investigate the shapes of three adhering vesicles with varying reduced volume in both strong and weak adhesion regimes. We explore two triplet topologies, the triangle and the linear one. In the triangle topology, each of the three vesicles is in contact with the other two, whereas in the linear topology the middle vesicle is sandwiched by two end vesicles. We study typical morphological changes of both types of vesicle triplets at various reduced volumes and adhesion strengths. The obtained morphologies are examined using energy models composed of the bending energy, surface energy, and adhesion energy. The equilibrium shapes of triplets are computed by minimizing the total energy using the Surface Evolver package (hereafter abbreviated as SE)[27] modified so as to apply to adhering vesicles.[17] By combining systematic experiments and simulations, we reveal the various mechanisms that determine the morphology of vesicle triplets, especially focusing on the shape of the contact zone.

2 The model

2.1 Mechanical model of vesicle triplets: two-tension model

The total energy of the vesicle triplet W_{tt} is a sum of the local bending energy of vesicle i (i = 1, 2, 3), $W_{b,i} = (k_c/2)\int(C_{1,i} + C_{2,i})^2 dA_i$ [k_c is the bending rigidity and $C_{j,i}$ (j = 1 or 2) is the principal curvature], the surface energy $W_i^{sur} = T_i|A_i - A_{0,i}|$ (T_i is the surface tension, A_i is the actual vesicle area and $A_{0,i}$ is the preferred vesicle area), and the adhesion energy between vesicle i and j which reads $W_{i,j}^{ad} = -\Gamma A_{i,j}^c$ ($\Gamma > 0$ represents the adhesion strength and $A_{i,j}^c$ is the contact area).[17] First, we adopted the two-tension model where the surface tension in the non-contact zone (T^{nc}) is different from that in the contact zone (T^c), since the number density of lipid molecules in the contact zone is higher than that in the non-contact zone due to attractive inter-membrane interactions. In this case, the areas of vesicles in an aggregate are variable rather than fixed, and they are controlled by tensions. The total energy of the two-tension model is given by

$$W_{tt} = \sum_i W_{b,i} + \sum_i T_i^{nc} A_i^{nc} + \sum_i \sum_j^{ad} T_i^c A_{ij}^c - \sum_i \sum_{j>i}^{ad} \Gamma A_{ij}^c$$
$$= \sum_i W_{b,i} + \sum_i T_i^{nc} A_i^{nc} + \sum_i \sum_j^{ad} \left(T_i^c - \frac{\Gamma}{2}\right) A_{ij}^c \tag{1}$$

where $\sum_i \sum_j^{ad}$ means summing over vesicles j adhering to vesicle i, and the constant term is disposed of. Here we assume that the contact-zone tensions are the same in all vesicles and so are the non-contact-zone tensions, *i.e.*, $T_i^{nc} = T^{nc}$ and $T_i^c = T^c$. We normalize the total energy W_{tt} by the bending energy of a spherical vesicle (equal to $8\pi k_c$) so that the dimensionless

energy of the triplet reads

$$w_{tt} = \frac{W_{tt}}{8\pi k_c} = \sum_i w_{b,i} + \sum_i t_i^{nc} a_i^{nc} + \sum_i \sum_j^{ad} \left(t_i^c - \frac{\gamma}{2}\right) a_{ij}^c \tag{2}$$

where $w_{b,i} = (1/4)\int(c_{1,i} + c_{2,i})^2 da_i$ is the normalized bending energy; here $c_{j,i} = C_{j,i} R_{s,i}$ (j = 1 or 2) is the dimensionless principal curvature scaled by a characteristic length $R_{s,i} = \sqrt[3]{3V_i/4\pi}$. V_i is the vesicle volume. Then the vesicle area is normalized to $\int da_i = \int dA_i/4\pi R_{s,i}^2$, $a_i^{nc} = A_i^{nc}/4\pi R_{s,i}^2$, $a_{ij}^c = 2A_{ij}^c/4\pi(R_{s,i}^2 + R_{s,j}^2)$. The reduced surface tension for the non-contact and contact zone is defined by $t^k = T^k R_{s,i}^2/2k_c$ (k = nc or c). Similarly, the reduced adhesion strength between vesicle i and vesicle j reads $\gamma = \Gamma(R_{s,i}^2 + R_{s,j}^2)/4k_c$. For convenience, we express w_{tt} as

$$w_{tt} = \sum_i w_{b,i} + \gamma \sum_i \left[\left(\alpha - \frac{1}{2}\right) \sum_j^{ad} a_{ij}^c + \beta a_i^{nc}\right] \tag{3}$$

where $\alpha = t^c/\gamma$ and $\beta = t^{nc}/\gamma$. It should be noted that to obtain a physically meaningful solution, α should satisfy inequality $\alpha > 1/2$. The shapes predicted by the two-tension model are systematically examined by varying α and β at fixed γ.

3 Materials and methods

3.1 Chemicals

The phospholipid, 1,2-dimyristoyl-*sn-glycero*-3-phosphocholine (DMPC) (purity > 99%), was purchased from Avanti Polar Lipids (Alabaster, AL) and used without further purification. The vesicles were labeled with a fluorescent phospholipid, Texas Red™ 1,2-dihexadecanoyl-*sn-glycero*-3-phosphoethanolamine (TR-DHPE), purchased from Thermo Fisher Scientific (Waltham, MA). The repulsive electrostatic interaction between DMPC vesicles was screened by adding potassium chloride (KCl) purchased from Wako Pure Chemicals Industries (Osaka, Japan). To adjust the osmolarity between the inside and outside of vesicles, we used fructose purchased from Sigma-Aldrich Japan (Tokyo, Japan). For the preparation of vesicle suspensions, we used ultrapure water purified with a Direct-Q 3 UV water purification system (Merck Millipore, Darmstadt, Germany).

3.2 Vesicle preparation

Vesicles were prepared using the gentle hydration technique.[28] First, 7 μL of a chloroform solution of DMPC (10 mg mL⁻¹) and 0.15 μL of a chloroform solution of TR-DHPE (1 mg mL⁻¹) were well mixed in a test tube with 50 μL of pure chloroform solution. Then we evaporated the organic solvent in a stream of nitrogen gas, and the obtained lipid film was kept under vacuum for one night to completely remove the remaining solvent. To adjust the osmolarity, the dried lipid film was hydrated with 1 mL of fructose solution having a desired concentration at 50 °C for half a day. During the hydration process, the lipid films spontaneously form a GUV suspension, where the diameters of the GUVs are 10–60 μm.

3.3 Preparation of vesicle triplets

In general, DMPC vesicles show no spontaneous adhesion due to the repulsive electrostatic interaction.[17] In this study, vesicle adhesion is attained by controlling the intermembrane interaction, which consists of van der Waals attraction, electrostatic repulsion, and undulation (Helfrich) repulsion. Vesicle aggregation is induced by enhancing the screening of electrostatic repulsion. The procedure for the preparation of vesicle triplets is as follows. First, the microscope observation chamber was filled with a KCl solution of the desired concentration (100 mM for weak adhesion and 200 mM for strong adhesion); KCl was chosen so as to minimize the effects of ion binding to the DMPC headgroup.[29] Then, we picked up 10 or more spherical vesicles of diameters between 10 and 30 μm from the vesicle suspension using a micropipette with an inner diameter of 60 μm (Vacu Tip II; Eppendorf, Hamburg, Germany), and carefully transferred them into the KCl solution in the chamber. After the transfer, we sealed the chamber using a coverslip to avoid evaporation of water. The vesicles spontaneously formed doublets, triplets, and larger aggregates. Among them, triplets consisting of vesicles having the same size were selected and used for further examination.

3.4 Observation of morphology changes of vesicle triplets with varying reduced volume

In this study, we investigated shapes of vesicle triplets with varying reduced volume, which is attained by thermal area expansion of the DMPC membrane.[30] The thermal area expansion coefficients of the DMPC membrane in pure water, and 100 mM and 200 mM KCl solutions are 0.004, 0.011, and 0.0012 K^{-1}, respectively.[17] Using the thermal area expansion $\varepsilon = A^{-1}\mathrm{d}A/\mathrm{d}T$ (A: area of membrane), the temperature dependence of the reduced volume is expressed by

$$v = v_0 \exp\left(-\frac{3}{2}\varepsilon(T - T_0)\right) \tag{4}$$

where v_0 is the reduced volume at $T = T_0$. The sealed sample chamber was set on a temperature-controlled stage for microscopic observation (PE120; Linkam Scientific Instruments, Tadworth, UK). Then we increased the temperature from 25 to 45 °C at a rate of 1 °C min^{-1}. The deformation of vesicle triplets caused by heating was monitored using an Axio Observer Z1 inverted fluorescence microscope (Carl Zeiss, Oberkochen, Germany) with a 20× objective (LD Plan-Neofluar, NA, 0.40) and recorded using a Complementary Metal-Oxide-Semiconductor (CMOS) camera ORCAFlash 4.0 (Hamamatsu Photonics, Hamamatsu, Japan).

3.5 Analysis of triplet morphologies using Surface Evolver

The theoretical triplet shape was analyzed using the SE package. In SE, the surface of a vesicle is represented by a triangular mesh. To describe adhering vesicles, we imposed a geometrical constraint that fixes the distance between the adhesion zones of contacting vesicles.[17] The equilibrium shapes were obtained by minimizing the total energy.

4 Results

4.1 Shape transformation of vesicle triplet with triangular topology in strong adhesion regime

In a previous paper, we showed the shape transformation of vesicle doublets in the strong adhesion regime (KCl 200 mM) by increasing the temperature from 25 to 38 °C, where a vesicle doublet composed of spherical caps and a flat contact zone deforms into a compact sphere shape with a flat contact zone and then the flat contact zone transforms into a sigmoidal shape.[17] When the vesicle aggregate changes from a doublet to a triplet, the topology plays an important role. Here we demonstrate the shape transformation of the triplet with a triangular topology in 200 mM KCl solution (strong adhesion regime) by heating from 25 to 45 °C as shown in Fig. 1a (Movie S1, ESI†). The initial triplet was composed of three spherical caps with a trifurcated flat contact zone (25 °C), where the three interfaces meet at an intersection with angles of 120°, similar to the Plateau rules. Upon increasing the temperature, the area of the contact zone increased while the zone itself remained flat, and the whole shape of the triplet transformed into a compact spherical shape (30 °C). Upon further heating, the flat contact zone bends to a half-wave shape (45 °C). In each vesicle, a pair of invaginating and protruding half-wave shapes adhered to other vesicles to form the so-called sigmoidal contact zone. Hereafter we refer to this structure as the "Three-Tomoe" pattern due to its similarity to the traditional Japanese emblem (Fig. 1b). In this sigmoid-contact triplet, the combined area of the contact zones is as large as possible due to the strong adhesion, resulting in a minimum area of the non-contact zone, *i.e.*, the compact spherical shape with a sigmoidal contact zone. Note that at microscopic resolution, the compact triplet forms a notchless rim between the contact and non-contact zones. When we conducted the shape transformation in five different instances of vesicle triplets, three triplets showed the Three-Tomoe pattern, whereas the remaining two instances showed irregular curved contact zones. This is presumably because of the variation of the area, volume, and lamellarity across vesicles.

4.2 Simulation using a two-tension model

The morphology change observed in the strongly-adhering triplet with a triangular topology (Fig. 1a) is analogous to that in the strongly-adhering doublet. To describe the vesicle triplet morphologies, we first adopted the two-tension model [eqn (3)] which was developed to describe the vesicle doublet (Section 2.1). The equilibrium shapes of triplets obtained by minimizing the total energy of the two-tension model are shown in Fig. 1c, where α is varied from 2.0 to 1.0 at $\beta = 2.0$ and $\gamma = 100$ (strong adhesion regime). The mean reduced volume of the triplet can be estimated by $\bar{v} = (v_1 + v_2 + v_3)/3$ and is indicated at the bottom of each computed triplet shape. At $\alpha = 2.0$ and $\beta = 2.0$ ($\bar{v} = 0.95$), the triplet consists of three spherical caps with a trifurcated flat contact zone, which describes well the observed triplet at 25 °C in Fig. 1a. As α decreases, the triplet develops into a compact shape with decreasing $\bar{v}$, reaching a completely spherical shape

(a)

(b)

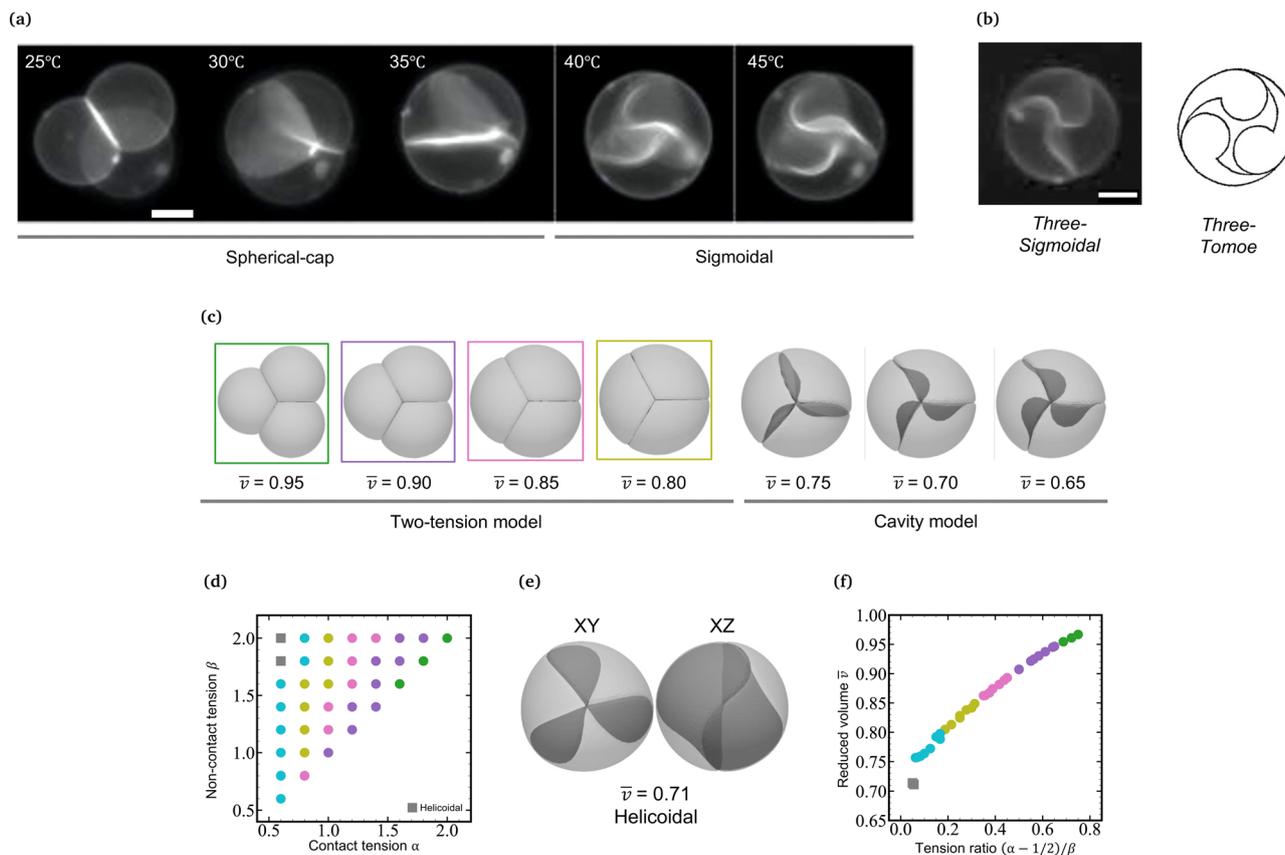**(c)**

(d)   **(e)**   **(f)**

Fig. 1 Shape transformation of vesicle triplets with a triangular topology in the strong adhesion regime. (a) Fluorescence microscopy images of vesicle triplets with a triangular topology in KCl 200 mM solution upon heating from 25 °C to 45 °C. The deformation process is divided into two stages, the first one characterized by spherical-cap triplets with flat contact zones and the second one including compact spherical triplets with sigmoidal contact zones. (b) Another view of the compact spherical triplet with sigmoidal contact zones (left) and the schematic representation of the "Three-Tomoe" pattern (right). (c) Shape change of vesicle triplets with a triangular topology as a function of the mean reduced volume $\bar{v}$, which are reproduced by numerical simulations using the Surface Evolver package; left: two-tension model, right: cavity model. (d) Phase diagram of the two-tension model in the (α, β) plane. The mean reduced volume $\bar{v}$ of the triplet shapes is represented using color codes as follows: $\bar{v} = 0.95$ (green), 0.90 (violet), 0.85 (pink), 0.80 (dark yellow), and 0.75 (light blue). The gray square denotes helicoidal triplets shown in panel e. The triplet shapes in panel c characterized by the above color-codes correspond to the colored domains in the phase diagram in panel d. (e) Helicoidal shape with $\bar{v} = 0.71$ obtained by the two-tension model (gray square in panel d). Left: XY plane and right: XZ plane. (f) Master curve of the mean reduced volume $\bar{v}$ vs. $(\alpha - 1/2)/\beta$, reconstructed from the phase diagram in panel d. Scale bars in microscopy images are 20 μm.

with a trifurcated flat contact zone at $\alpha = 1.0$ ($\bar{v} = 0.8$), which well reproduces the observed morphology at 30 °C in Fig. 1a. To visualize the dependence of the triangular triplets on α and β dependence within the two-tension model, we constructed a phase diagram (Fig. 1d) where the triplets are represented using color-coded dots according to their mean reduced volume: green ($0.95 \leq \bar{v} < 1.00$), violet ($0.90 \leq \bar{q}v < 0.95$), pink ($0.85 \leq \bar{v} < 0.90$), dark yellow ($0.80 \leq \bar{v} < 0.85$), and light blue ($0.75 \leq \bar{v} < 0.80$).

It is interesting to note that the mean reduced volume lies on a master curve when we plot $\bar{v}$ against $T_{c/nc} = (\alpha - 1/2)/\beta$ [see eqn (3)] as shown in Fig. 1e. Considering that the tension ratio reads $(\alpha - 1/2)/\beta = (t^c - \gamma/2)/t^{nc}$, the master curve in Fig. 1f indicates that the membrane area is determined by the force balance between the contact zone and non-contact zone. According to the Young-Dupré equation, the force balance between adhesion force and surface tension at the rim of the contact zone defines the contact angle. When it comes to the

trifurcated flat contact zone in vesicle triplets, the contact angle determines the surface area of the vesicle, i.e., reduced volume, since the vesicle volume remains constant during morphological changes. It should be noted that if the normalized adhesion strength decreases to $\gamma \approx 10$, the Young-Dupré equation is violated and the triplet morphology is dominated by the bending energy term in eqn (3). In this case, the triplet shape approaches the prediction of the model where the total energy is expressed by a sum of the vesicles' bending energies and adhesion energies with a constant vesicle surface area and volume constraints.

As α is further decreased below 1.0, the contact zone of the compact spherical triplet is gradually deformed as shown in Fig. 1e ($\alpha = 0.6$ and $\beta = 2.0$). A careful inspection of Fig. 1e reveals that this interface is a helicoidal shape rather than the sigmoidal shape observed in the experiments; the edge of the helicoidal contact zone is twisted. The compact spherical triplets with the helicoidal contact zone appear at small α and

large β (gray squares: α = 0.6, β = 1.8 and 2.0 in Fig. 1d) and the flat-interface triplets transform into helicoidal-interface triplets discontinuously at $T_{c/nc} \approx 0.05$ (Fig. 1f). In this theoretical framework, however, we cannot reproduce the compact vesicle triplet with a sigmoidal contact zone. Numerical energy minimization produced the same helicoidal equilibrium morphology even if the initial shape did have a sigmoidal contact zone. For comparison with another framework, the area-fixed model was introduced into the same reduced volume, resulting in oblate-based vesicle triplets (ESI:† Fig. S1).

4.3 Cavity model

In the compact sphere triplet region ($\bar{v} < 0.8$), the total area of non-contact zones should be equal to $4\pi R_{cav}^2$, where $R_{cav} = \sqrt[3]{3(V_1 + V_2 + V_3)/4\pi}$ due to the strong tension at the non-contact zone ($T_{c/nc} \approx 0.05$). Thus, the discontinuous decrease of the reduced volume observed in the two-tension model means abrupt expansion of the membrane area in the contact zone to minimize the adhesion energy in eqn (1). However, this abrupt expansion of the membrane area is unrealistic as the membrane cannot be stretched beyond a certain point. To construct a model of strongly adhering vesicles, we impose geometrical constraints that the total membrane area and volume of triplet vesicles are constant, and the total area of the non-contact zones is bounded by $4\pi R_{cav}^2$ for the compact spherical triplets. This geometrical constraint for the non-contact zone is expressed by additional potential $U_{cav}(r) = \infty$ for $|r| > R_{cav}$ otherwise $U_{cav}(r) = 0$. In SE, the vertices of the triangular mesh representing the vesicle surface are restricted to a sphere of radius R_{cav}. This effectively corresponds to an infinite potential at $|r| > R_{cav}$. The total energy of the cavity model for the vesicle triplet is given by

$$w_{cav} = \sum_i w_{b,i} - \sum_i \sum_j^{ad} \gamma a_{ij}^c + U_{cav}(\mathbf{r}) \tag{5}$$

where the surface energy terms in eqn (3) are omitted due to the constant-area constraint.

We minimize the total energy of the cavity model using SE as a function of $\bar{v}$ as shown in Fig. 1c ($0.65 \leq \bar{v} < 0.75$). Note that we set the adhesion strength at $\gamma = 10$, which is smaller than that of the two-tension model ($\gamma = 100$) due to the geometrical constraint. The cavity model reproduces well the compact spherical triplets with a sigmoidal contact zone observed in experiments. With a decrease in reduced volume, the magnitude of the sigmoidal deformation increases, which agrees well with the observed temperature dependence of the sigmoidal interface (40 and 45 °C in Fig. 1a). The switch from the two-tension model to the cavity model, corresponding to the transition from the flat interface to the sigmoidal interface, takes place between $\bar{v}$ = 0.80 and 0.75 (Fig. 1c). Note that the completely spherical triplet with a trifurcated flat contact zone has a mean reduced volume of $\bar{v} \approx 0.78$. By combining the two-tension model with the cavity model, we can reproduce a series of morphological changes observed in the strongly-adhering vesicle triplets with a triangular topology.

4.4 Shape transformation of triplets with a linear topology in the strong adhesion regime

In the linear topology, triplets are composed of a pancake-shaped vesicle sandwiched by two spherical-cap vesicles. Thus, the middle vesicle is not identical to the end vesicles. Here we show the shape transformation of the vesicle triplet with a linear topology in 200 mM KCl solution (strong adhesion regime) by heating from 25 to 45 °C in Fig. 2a (Movie S2, ESI†). The initial triplet had parallel flat contact zones (25 °C). With an increase in temperature, the areas of the contact zones increased, and simultaneously the pancake-shaped middle vesicle became wedge-like (30 °C). At 35 °C, the triplet transformed into a compact, virtually spherical shape with two flat contact zones. Upon further heating, the middle vesicle assumed a biconvex shape (37 and 44 °C). We studied five instances of triplets, and all of them showed the reported shape transformation from a pancake-shaped vesicle sandwiched between two spherical-cap vesicles to a compact spherical shape with biconvex interfaces. Note that if the linear triplet is L-shaped, it undergoes a topological transition to a triangular triplet upon heating once and the contact between the two end vesicles is established (not shown).

4.5 Simulations of two-tension and cavity models

The morphology of the linear triplets with flat contact zones is nicely reproduced by the two-tension model. Like in the triangular triplet, the numerical simulation using SE started at α = 2.0 and β = 2.0 (γ = 100 where the model predicts a $\bar{v}$ = 0.95 linear triplet with parallel flat contact zones shown in Fig. 2b, which is geometrically consistent with experimental observations. As α is decreased at β = 2.0, the area of the flat contact zone increases, and at α = 1.4 ($\bar{v}$ = 0.85 in Fig. 2b) the middle vesicle deforms into a wedge shape, which also agrees with observations (30 °C in Fig. 2a). By further decreasing α, the wedge angle of the middle vesicle decreases and the whole shape becomes more isometric and compact (α = 1.0, $\bar{v}$ = 0.75). As α is further decreased below 1.0, the simulation gives collapsed self-intersecting non-physical shapes, indicating that the two-tension model is no longer applicable. To visualize the dependence of the flat-contact linear triplets on α and β, we construct a phase diagram (Fig. 2c), which is color-coded just like that of the triangular triplets in Fig. 1d. The morphology map for the linear triplet in the (α, β) plane is very similar to that for the triangular triplet (Fig. 1d). In the $\bar{v}$ against $T_{c/nc}$ plot, all points fall on a master curve (Fig. 2d), which has a slightly larger slope than that for the triangular triplet since the middle vesicle has a smaller reduced volume. The master curve terminates at $T_{c/nc}$ = 0.23 ($\bar{v}$ = 0.75) where the two-tension triplets collapse. For comparison with another framework, the area-fixed model was introduced into the same reduced volume, resulting in oblate-based vesicle triplets (ESI:† Fig. S2).

From this point on, we switched to the cavity model which nicely reproduces compact triplets with a biconvex middle vesicle ($\bar{v}$ = 0.65 in Fig. 2b). The transition from flat-contact triplets
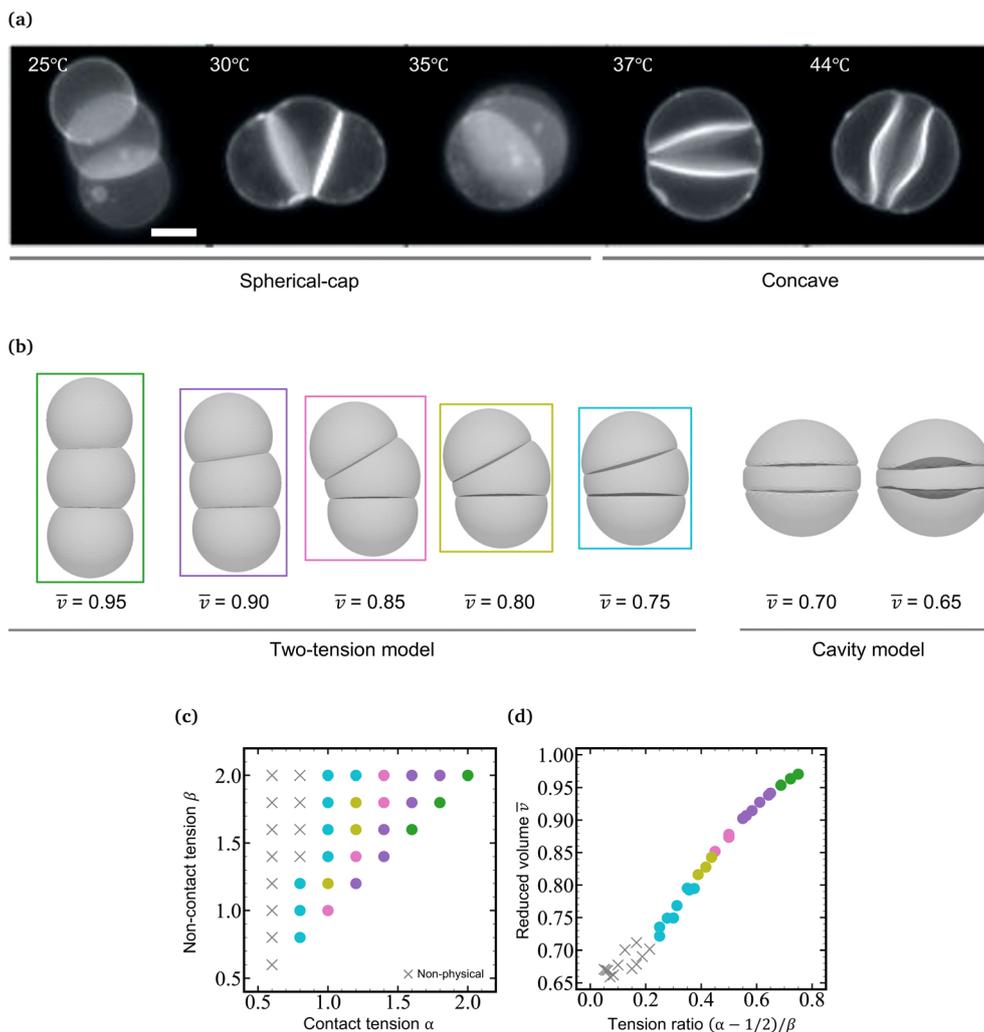
Fig. 2 Shape transformation of vesicle triplets with a linear topology in the strong adhesion regime. (a) Fluorescence microscopy images of vesicle triplets with a linear topology in KCl 200 mM solution upon heating from 25 °C to 44 °C. The deformation process is divided into the spherical-cap, flat-contact-zone triplet stage and the compact, biconvex-contact-zone triplet stage. (b) Shape change of vesicle triplets with a linear topology as a function of $\bar{v}$, which are reproduced by numerical simulations using the Surface Evolver package; left: two-tension model, right: cavity model. (c) Phase diagram of the two-tension model in the (α, β) plane. Triplet shapes are color-coded like in Fig. 1d, with crosses indicating collapsed shapes. The triplet shapes in panel b are characterized by colored domains in the phase diagram in panel c. (d) Master curve of the mean reduced volume $\bar{v}$ vs. $(\alpha - 1/2)/\beta$, reconstructed from the phase diagram in panel c. Scale bars in microscopy images are 20 μm.

(reproduced by the two-tension model) to biconvex-contact triplets (reproduced by the cavity model) takes place at a mean reduced volume between $\bar{v}$ = 0.70 and 0.65, which is consistent with the geometrical prediction of $\bar{v} \approx 0.68$ for a linear triplet which has a perfectly spherical external form and consists of vesicles of identical volumes with flat contact zones.

4.6 Morphology transition of vesicle triplets in the weak adhesion regime

Here we examine the morphology transition of vesicle triplets in the weak adhesion regime (KCl 100 mM). In the case of the triangular topology (Fig. 3a and Movie S3, ESI†), the initial morphology at 25 °C consists of three spherical caps with a trifurcated flat contact zone, identical to that observed in the strong adhesion regime. As the temperature increases, the

triplets deformed into a compact shape with a trifurcated flat contact zone (30 °C). Upon further heating, however, each spherical-cap vesicle transformed into a prolate shape while keeping contact with the other two vesicles (35 °C), and eventually the triplet consisted of cigar-shaped vesicles (45 °C). For the linear topology in the weak adhesion regime (Fig. 3b and Movie S4, ESI†), the initial triplet shape at 25 °C was similar to that in the strong adhesion regime. With an increase in temperature, the middle vesicle deformed into a wedge shape and the linear arrangement transformed into an L-shaped arrangement (30 °C). On further heating, the vesicle shapes gradually became prolate (35 °C) until the triplet consisted of three parallel vesicles (40 and 45 °C). Like in the strong adhesion regime, we monitored the shape transformation in five linear and five triangular triplets in the weak adhesion
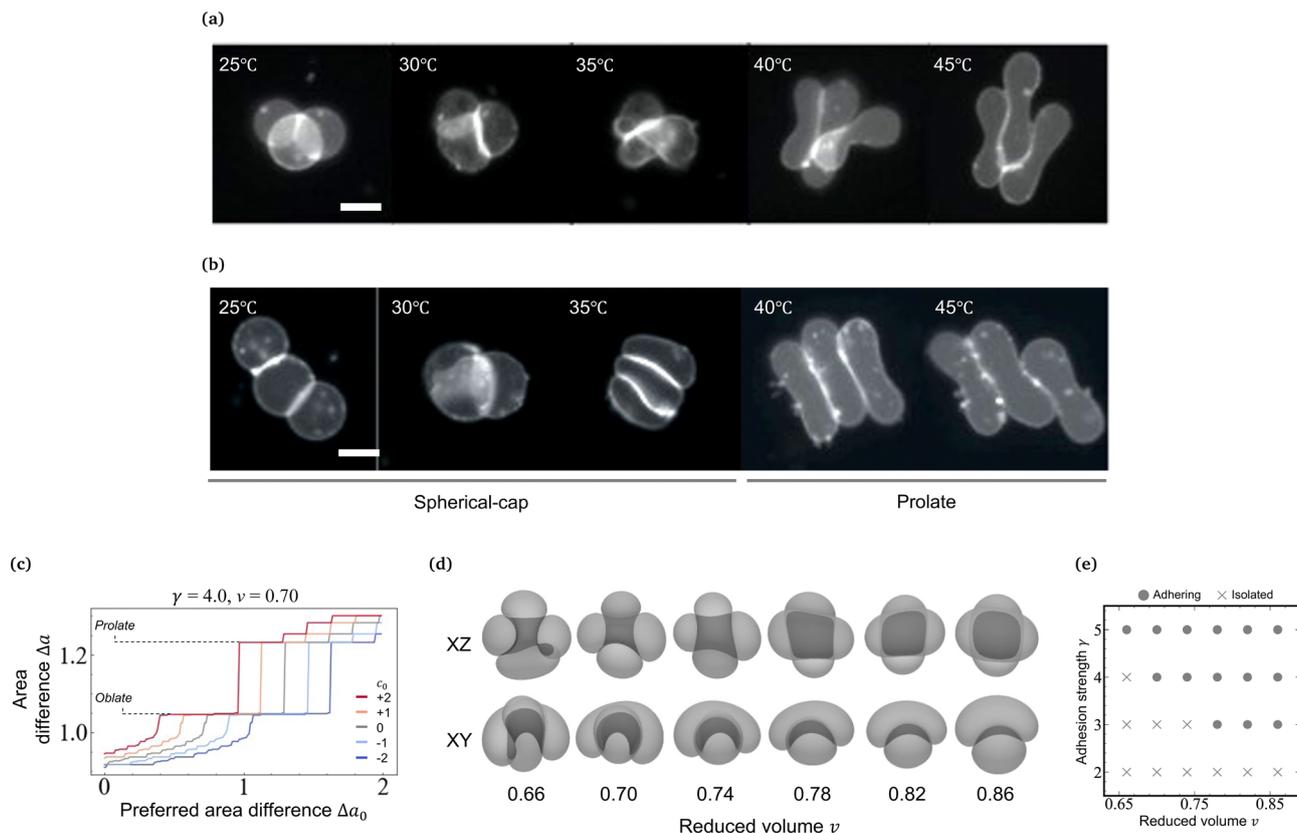
Fig. 3 Shape transformation of vesicle triplets in the weak adhesion regime. (a) Fluorescence microscopy images of vesicle triplets with a triangular topology in KCl 100 mM solution upon heating from 25 °C to 45 °C. The deformation process is divided into two stages: The spherical-cap, flat-contact-zone triplet stage and the prolate-vesicle triplet stage. (b) Fluorescence microscopy images of vesicle triplets with a linear topology in KCl 100 mM solution upon heating from 25 °C to 45 °C. The deformation process is divided into the spherical-cap, flat-contact-zone triplet stage and the prolate-vesicle triplet stage. (c) Preferred monolayer area difference (Δa_0) *versus* area difference (Δa) plot for various reduced spontaneous curvature c_0 obtained by the ADE-SC model with $\gamma = 4.0$, $v = 0.70$. The prolate and the oblate vesicle have $\Delta a = 1.22$ and 1.06, respectively. (d) Simulated prolate-based vesicle doublet images as a function of the reduced volume obtained by the ADE-SC model with $c_0 = 2.0$ and $\gamma = 5$. Doublet images are displayed in *XZ* projection (top) and *XY* projection (bottom), where the gray region shows the contact zone. (e) Stability diagram of the prolate based doublet (gray circle) and isolated two prolate vesicles (cross) in the (v,γ) plane obtained by the ADE-SC model with $c_0 = 2.0$. Scale bars in microscopy images are 20 μm.

regime, and all instances of each topology consistently showed the same shape transformation except for minor variations in the final state expected due to weak adhesion strength. In the triangular and linear topologies, each vesicle slid along the interface during the shape transformation and no separation of the vesicles was observed. Recalling that vesicle doublets in the weak adhesion regime transform into the parallel prolate morphology, we conclude that the stable shape of aggregates in the weak adhesion regime is based on prolate rather than on oblate vesicles.

4.7 Theoretical interpretation of prolate-vesicle aggregates

As temperature increases, the undulation repulsion force increases (due to the increase of amplitude to membrane fluctuations), which results in a decrease of the adhesion strength.[17] In the weak adhesion regime, however, since the membrane tension in the contact zone is weak, the excess membrane area produced by thermal expansion enhances the membrane fluctuations in the contact zone, which decreases the adhesion strength. Thus, the total energy in the weak

adhesion regime is expressed by

$$w_{\text{weak}} = \sum_i w_{\text{b},i} - \sum_i \sum_j^{\text{ad}} \gamma a_{ij}^{\text{c}} \qquad (6)$$

where the total vesicle volume and membrane area are fixed. The phase behavior of vesicle doublets whose total energy is given using eqn (6) was investigated in detail.[14–16] In the weak adhesion regime, the simulation studies predict that the doublets with $0.6 < v < 0.8$ deform to the aggregates of oblate shape. Here we examine the discrepancy between the theoretical prediction and experimental observations. When the contribution of the bending energy is subdominant, we express the bending term for simplicity just by the local bending energy, whose dimensionless form reads $w_{\text{b},i} = (1/4)\int(c_{1,i} + c_{2,i})^2 \mathrm{d}a_i$.[31] However, when the total energy is dominated by the bending energy, an appropriate model for describing the morphology of a single vesicle is the area-difference elasticity (ADE) model,[32–35] whose energy is expressed by the local-bending energy term and the non-local bending energy term

$W_{\mathrm{ADE}} = (k_{\mathrm{c}}/2)\int(C_1 + C_2)^2 \mathrm{d}A + k_{\mathrm{r}}/(2Ah^2)(\Delta A - \Delta A_0)^2$, where k_{r} is the non-local bending modulus and h is the distance between the monolayers' neutral planes. Here $\Delta A = h\int(C_1 + C_2)\mathrm{d}A$ and $\Delta A_0 = (N^+ - N^-)a$ are the area difference between the two monolayers and the preferred area difference, respectively, where N^+ and N^- are the number of lipid molecules in the outer and inner monolayers, and a is the cross-sectional area of a lipid. According to the ADE model, the vesicle shape is determined by the reduced volume v and the preferred area difference ΔA_0. The ADE model predicts that in the $0.6 < v < 0.8$ region, the stable vesicle shape is oblate. To stabilize the prolate vesicle, we have to adjust ΔA_0 by introducing spontaneous curvature, which is expressed by area-difference-elasticity and spontaneous curvature (ADE-SC) model.[36,37] The dimensionless energy of the ADE-SC model is given by

$$
\begin{aligned}
w_{\mathrm{ADE-SC}} &= \frac{1}{4}\int(c_1 + c_2)^2 \mathrm{d}a + q(\Delta a - \Delta \tilde{a}_0)^2 \\
&\quad - c_0 \Delta \tilde{a}_0 + \left(1 + \frac{1}{q}\right)\frac{c_0^2}{4}
\end{aligned}
\tag{7}
$$

where $q = k_{\mathrm{r}}/k_{\mathrm{c}}$ is the ratio of non-local and local bending moduli (in this study we use $q = 3$),[38,39] $c_0 = R_{\mathrm{s}}C_0$ is the reduced spontaneous curvature, $\Delta a = \Delta A/8\pi h R_{\mathrm{s}}$ and $\Delta a_0 = \Delta A_0/8\pi h R_{\mathrm{s}}$ are the reduced monolayer area difference and preferred reduced monolayer difference, respectively, and $\Delta \tilde{a}_0 = \Delta a_0 + c_0/2q$ is the preferred area difference renormalized by the spontaneous curvature. Thus, the range of Δa_0 where prolate shapes are stable is shifted by $c_0/2q$. From the experimental point of view, the size asymmetry of solute molecules between the inside and outside of the vesicles causes a depletion-induced spontaneous curvature of $c_0 \approx 1.5$ (inside: fructose and outside: KCl).[40-42] For simplicity, here we addressed the stability of the prolate-based doublet using the ADE-SC model. In this scheme, the total energy is given by

$$
w_{\mathrm{weak,ADE-SC}} = \sum_i w_{\mathrm{ADE-SC},i} - \sum_i \sum_j^{\mathrm{ad}} \gamma a_{ij}^{\mathrm{c}}
\tag{8}
$$

Now, we have four parameters $(\Delta a_0, c_0, \gamma, v)$ to explore the phase behavior of this model. Here, the phase boundary between the oblate-vesicle doublet and the prolate-vesicle doublet $\Delta a_0^{\mathrm{o/p}}$ is examined as a function of c_0. For example, the reduced monolayer area difference of the stable vesicle Δa is plotted against the preferred reduced monolayer difference Δa_0 at $(\gamma, v) = (4.0, 0.70)$ for various c_0 values in Fig. 3c. At $v = 0.70$, the oblate vesicle and prolate vesicle have $\Delta a = 1.06$ and 1.22, respectively. For $c_0 = 0$, the stable vesicle shape is transformed from oblate to prorate at $\Delta a_0 = 1.3$, i.e., the phase boundary is at $\Delta a_0^{\mathrm{o/p}} = 1.3$. Considering that Δa_0 of the initial vesicles is close to 1.0 as implied by their generally round shapes, the doublets prefer the oblate-vesicle shape, which is consistent with the prediction of the energy model expressed using eqn (6). Upon increasing c_0, the phase boundary shifts toward lower Δa_0, i.e., $\Delta a_0^{\mathrm{o/p}} = 1.03$ for $c_0 = 1.0$ and $\Delta a_0^{\mathrm{o/p}} = 0.86$ for $c_0 = 2.0$. Thus, if the vesicle has $c_0 > 1.5$, the doublet prefers the prolate-vesicle shape at $(\Delta a_0, \gamma, v) = (1.0, 4.0, 0.70)$. However, the simulations using eqn (8) show

that the prolate doublets do not consist of parallel vesicles as observed in experiments (Fig. 3a and b), but have a compact crossed shape as shown in Fig. 3d. In Fig. 3d, we show prolate doublets with $c_0 = 2.0$ and $\gamma = 5$ at various reduced volumes obtained by the ADE-SC model. With a decrease in v, the compact crossed prolate doublets deform so as to increase the contact area at the expense of the bending energy. To obtain a parallel prolate doublet, the adhesion strength should thus be reduced. However, in such a very weak adhesion regime we have to consider two isolated vesicles as another stable-state candidate. Therefore, we compare the total energy of the adhering prolate-vesicle doublet and two isolated vesicles as a function of adhesion strength γ and reduced volume v at $c_0 = 2.0$. The obtained stable states (adhering prolate doublet or two isolated vesicles) are mapped into (v, γ) space as shown in Fig. 3e. The aggregation transition takes place at γ between 3 and 5, and the prolate-vesicle doublets just before the transition have compact crossed shapes shown in Fig. 3d. Based on these arguments, we conclude that in the observed prolate-vesicle triplets are probably not minimal-energy structures but metastable.

5 Discussion

Here we focus on curved interfaces observed in a compact spherical triplet (cavity model regime). In compact triplets, the non-contact zones form a spherical external surface, and the excess area produced by thermal expansion is used to deform the contact zones. The excess membrane forms a sigmoidal interface for triangular triplets (Fig. 1b), whereas a convex interface is observed for linear triplets (Fig. 2a). According to the cavity model [eqn (5)], the shape of the interface is governed by the bending energy under the constraints of a fixed vesicle volume and area.

On the one hand, in the triangular triplets, all vesicles are identical and have two contact zones. There are two modes to deform the contact zone as the membrane expands upon heating. One is the sigmoidal mode where the edge of the contact zone is fixed, and the contact zone forms the half-wave shape (cavity model; Fig. 1c). Another one is the helicoidal mode where the edge of the contact zone is twisted and the contact zone forms a helicoid surface (two-tension model; Fig. 1e). In the experiments, we observe the sigmoidal mode as shown in Fig. 1a. The helicoidal mode appears in the two-tension model, where the reduced volume is discretely decreased ($v = 0.75$ to 0.71) at the flat to helicoid transition as shown in Fig. 1f. Since the volume of the vesicle is constant during the transition, this abrupt change in the reduced volume implies a discontinuous increase in the area of the vesicle membrane by 8.6%. However, due to the high area expansion modulus of the phospholipid membrane (~ 250 mN m^{-1}),[43] such a drastic increase in the membrane area is not permitted. This membrane area constraint is imposed within the cavity model. Therefore, we observe the half-wave deformation of the contact zone as predicted by the cavity model. In addition, the volume

change due to the half-wave deformation of the contact zone must be cancelled in each vesicle. This volume conservation results in a "Three-Tomoe" triplet, where each vesicle has a protruding contact zone and an invaginating contact zone (*i.e.*, sigmoidal deformation) as shown in Fig. 1b.

On the other hand, in the linear triplets, the end vesicles have a single contact zone whereas the middle vesicle has two contact zones. In this case, the excess area used for the contact zone is different between the end vesicles and the middle vesicle. The excess area due to thermal expansion is the same in each vesicle, but in the end vesicles it is engaged in a single contact zone, whereas in the middle vesicle it is distributed between two of them. Therefore, in the contact zone, the excess area of the end vesicle is larger than that of the middle vesicle, which causes the membrane to protrude toward the end vesicle as shown in Fig. 2a. The middle vesicle deforms into a biconvex shape and the end vesicles deform into a stomatocyte shape while keeping their volume constant. It should be noted that in the linear topology, the edge of the contact zone is fixed as well.

In summary, the shape of the interface in compact doublets and triplets is determined under vesicle volume conservation conditions. For a single interface, the interface shape is governed by the area difference of the contact zone. If the contact area of each vesicle is the same, the contact zone is deformed into a sigmoidal shape, whereas if the contact zone has an area difference between the adhering vesicles, the contact zone protrudes toward the vesicle having a larger contact area. For connecting interfaces, each interface deforms into a half-wave shape and the overall shape of the interface is sigmoidal due to volume conservation.

Based on the above deformation rule, we examined the interface shape of vesicle quartets having different topologies, *i.e.*, T-shape and linear (Fig. 4a and b). In the T-shape vesicle quartet, one spherical cap vesicle adheres to the triangular triplet (Fig. 4c). Two spherical cap vesicles in the triangular part have two contact zones, the remaining one sandwiched vesicle in the triangular part has three contact zones, and an end vesicle has a single contact zone. At the initial stage (25 °C in Fig. 4a), all contact zones in the T-shape vesicle quartet are flat. Upon increasing the temperature, the three contact zones in the triangular part deform into the sigmoidal shape to keep the vesicle volume constant so as to form a "*Three-Tomoe*" pattern, whereas the interface between the "*Tomoe*" vesicle and end vesicle protrudes toward the end vesicle (40 and 50 °C in Fig. 4a). This interface pattern agrees with the deformation rule. The linear quartet is composed of two spherical end vesicles and two pancake vesicles (Fig. 4c). Two spherical end vesicles have one contact zone, and two pancake vesicles have two contact zones. By increasing the temperature to 47 °C (Fig. 4b), the interface between the end and pancake vesicles protrudes toward the end vesicle, whereas the interface between two pancake vesicles shows a flat contact zone since
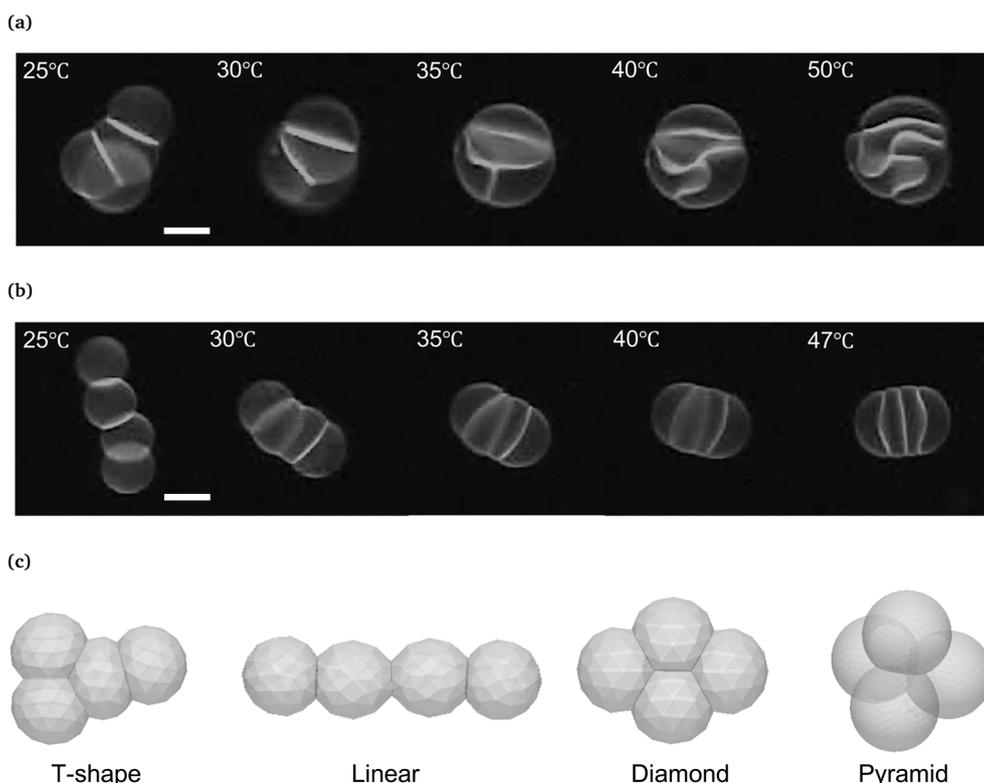

Fig. 4 Shape transformation of vesicle quartets in the strong adhesion regime. (a) Fluorescence microscopy images of vesicle quartets with a T-shaped topology in KCl 200 mM solution upon heating from 25 °C to 50 °C. (b) Fluorescence microscopy images of vesicle quartets with a linear topology in KCl 200 mM solution upon heating from 25 °C to 47 °C. (c) Various topologies of vesicle quartets; T-shape, linear, diamond, and pyramid. Scale bars in microscopy images are 20 μm.

the two sandwiched vesicles are identical. Again, the observed interface shapes in the linear vesicle quartet are consistent with our deformation rule, although the whole shape of the non-contact zones of the quartet is not spherical.

It should be noted that vesicle quartets have two other interesting topologies, *i.e.*, diamond and pyramid (Fig. 4c). In the diamond topology, two vesicles have three contact zones, and two vesicles have two contact zones, whereas the pyramid is composed of four identical vesicles with three contact zones. The three contact zones in a vesicle may produce frustrated interfaces to conserve the vesicle volume. Although we could not achieve these topologies experimentally, the deformations of vesicle quartets with topologies will reveal a geometrical law governing vesicle aggregates. To address these complex topologies, it might be practical to develop an efficient way for manufacturing vesicle aggregates by using optical tweezers or microfluidic devices.[44,45]

Finally, we mention that we also theoretically considered a wrapped topology where the inner vesicle is contained within two identical cup-like vesicles forming a shell.[46] In the strong adhesion regime, this topology is energy-wise more favorable due to a large contact area but only if the reduced volumes of the three vesicles are quite different from each other: In the inner vesicle, $v = 1$ whereas in the other two $v = 0.4$. Given that in this work we focus on vesicles of identical sizes, we did not explore this shape further. At the same time, we note that the vesicle size polydispersity will significantly affect all vesicle aggregate topologies—and so would the existence of multiple contact zones between any two vesicles in an aggregate (here we tacitly restricted the discussion to single contact zones).

6 Conclusion

When comparing the present study of vesicle triplets with our past investigations of doublets, one can readily realize the increased complexity of the morphologies involved as well as the phenomena at work, which is of course anticipated—and in retrospect justifies our step-by-step approach to the physics of vesicle aggregates. Our experimental findings show that by controlling the adhesion strength, the vesicles can be steered so as to form either compact aggregates or non-compact ones. In the former, the contact zones show characteristic curved shapes that are never observed in soap bubbles, which is determined by the conservation of vesicle volume and area difference in the contact zone. Systematic studies for interface geometry of a few vesicle aggregates will lead to general rules for curved interfaces, such as the Plateau rules for planar interfaces. In the latter, the membrane bending energy evidently is very important, and this supports an interesting prospect of non-compact multivesicular aggregate morphologies such as shells. Whether these expectations will be confirmed remains to be seen, and it is unclear what may be the smallest number of vesicles in an aggregate where the morphological rather than topological classification will prevail.

On the theoretical side, our study advances the understanding of the modeling of vesicle aggregates partly by providing additional support for the so-called two-tension model and partly by substituting it with the cavity model proposed here. Another important novelty stemming from the combination of the two models is that at least in the large-adhesion regime, the shape of vesicle aggregates is determined primarily by the reduced volume of the vesicles; in the cavity model, the reduced volume is the only control parameter whereas in the two-tension model it depends on the tensions. This finding may be helpful when further elaborating the theoretical description of the aggregates.

Altogether, the morphologies of vesicle triplets are governed by the reduced volume, the adhesion strength of vesicles and the topology of the triplets. The adhesion strength is determined by the balance of intermembrane interactions, *i.e.*, the electrostatic repulsion, van der Waals attraction, and undulation repulsion, which produces the surface tensions in the contact and non-contact zones through the force balance. Therefore, the reported morphological changes in the vesicle triplets are general ones that would be observed in other phospholipid vesicle triplets.

Author contributions

P. Z., Y. S., and M. I. conceived the presented idea and designed the experiments. T. C. carried out the experiments. T. C. and P. Z. developed the theoretical formalism. T. C. wrote the manuscript with support from P. Z. and M. I.

Conflicts of interest

There are no conflicts to declare.

Acknowledgements

References

1 D. L. Weaire and S. Hutzler, *The Physics of Foams*, Clarendon Press, 1999.
2 J. Plateau, *Statique expérimentale et théorique des liquides soumis aux seules forces moléculaires*, Gauthier-Villars, 1873.
3 U. Seifert, K. Berndl and R. Lipowsky, *Phys. Rev. A: At., Mol., Opt. Phys.*, 1991, **44**, 1182–1202.
4 U. Seifert, *Adv. Phys.*, 1997, **46**, 13–137.
5 P. B. Canham, *J. Theor. Biol.*, 1970, **26**, 61–81.

6 S. Svetina and B. Žekš, *Eur. Biophys. J.*, 1989, **17**, 101–111.

7 H. J. Deuling and W. Helfrich, *Biophys. J.*, 1976, **16**, 861–868.

8 G. H. W. Lim, M. Wortis and R. Mukhopadhyay, *Proc. Natl. Acad. Sci. U. S. A.*, 2002, **99**, 16766–16769.

9 D. Tilley, W. T. Coakley, R. K. Gould, S. E. Payne and L. A. Hewison, *Eur. Biophys. J.*, 1987, **14**, 499–507.

10 D. Flormann, O. Aouane, L. Kaestner, C. Ruloff, C. Misbah, T. Podgorski and C. Wagner, *Sci. Rep.*, 2017, **7**, 7928.

11 J. L. McWhirter, H. Noguchi and G. Gompper, *Proc. Natl. Acad. Sci. U. S. A.*, 2009, **106**, 6039–6043.

12 G. Tomaiuolo, L. Lanotte, G. Ghigliotti, C. Misbah and S. Guido, *Phys. Fluids*, 2012, **24**, 051903.

13 M. Brust, O. Aouane, M. Thiébaud, D. Flormann, C. Verdier, L. Kaestner, M. W. Laschke, H. Selmi, A. Benyoussef, T. Podgorski, G. Coupier, C. Misbah and C. Wagner, *Sci. Rep.*, 2014, **4**, 4348.

14 P. Ziherl and S. Svetina, *Proc. Natl. Acad. Sci. U. S. A.*, 2007, **104**, 761–765.

15 S. Svetina and P. Ziherl, *Bioelectrochemistry*, 2008, **73**, 84–91.

16 M. Hoore, F. Yaya, T. Podgorski, C. Wagner, G. Gompper and D. A. Fedosov, *Soft Matter*, 2018, **14**, 6278–6289.

17 K. Murakami, R. Ebihara, T. Kono, T. Chiba, Y. Sakuma, P. Ziherl and M. Imai, *Biophys. J.*, 2020, **119**, 1735–1748.

18 L. Parolini, B. M. Mognetti, J. Kotar, E. Eiser, P. Cicuta and L. Di Michele, *Nat. Commun.*, 2015, **6**, 5948.

19 L. Casas-Ferrer, A. Brisson, G. Massiera and L. Casanellas, *Soft Matter*, 2021, **17**, 5061–5072.

20 U. Seifert and R. Lipowsky, *Phys. Rev. A: At., Mol., Opt. Phys.*, 1990, **42**, 4768–4771.

21 J. Steinkühler, J. Agudo-Canalejo, R. Lipowsky and R. Dimova, *Biophys. J.*, 2016, **111**, 1454–1464.

22 J. Agudo-Canalejo and R. Lipowsky, *ACS Nano*, 2015, **9**, 3704–3720.

23 A. H. Bahrami, R. Lipowsky and T. R. Weikl, *Soft Matter*, 2016, **12**, 581–587.

24 Q. Yu, S. Othman, S. Dasgupta, T. Auth and G. Gompper, *Nanoscale*, 2018, **10**, 6445–6458.

25 H. T. Spanke, R. W. Style, C. François-Martin, M. Feofilova, M. Eisentraut, H. Kress, J. Agudo-Canalejo and E. R. Dufresne, *Phys. Rev. Lett.*, 2020, **125**, 198102.

26 E. J. Ewins, K. Han, B. Bharti, T. Robinson, O. D. Velev and R. Dimova, *Chem. Commun.*, 2022, **58**, 3055–3058.

27 K. A. Brakke, *Exp. Math.*, 1992, **1**, 141–165.

28 J. P. Reeves and R. M. Dowben, *J. Cell. Physiol.*, 1969, **73**, 49–60.

29 A. Cordom, O. Edholm and J. J. Perez, *J. Phys. Chem. B*, 2008, **112**, 1397–1408.

30 J. Käs and E. Sackmann, *Biophys. J.*, 1991, **60**, 825–844.

31 W. Helfrich, *Z. Naturforsch., C: Biochem., Biophys., Biol., Virol.*, 1973, **28**, 693–703.

32 B. Božič, S. Svetina, B. Žekš and R. E. Waugh, *Biophys. J.*, 1992, **61**, 963–973.

33 W. Wiese, W. Harbich and W. Helfrich, *J. Phys.: Condens. Matter*, 1992, **4**, 1647.

34 H.-G. Döbereiner, E. Evans, M. Kraus, U. Seifert and M. Wortis, *Phys. Rev. E: Stat. Phys., Plasmas, Fluids, Relat. Interdisc. Top.*, 1997, **55**, 4458–4474.

35 A. Sakashita, N. Urakami, P. Ziherl and M. Imai, *Soft Matter*, 2012, **8**, 8569–8581.

36 L. Miao, U. Seifert, M. Wortis and H. G. Döbereiner, *Phys. Rev. E: Stat. Phys., Plasmas, Fluids, Relat. Interdisc. Top.*, 1994, **49**, 5389–5407.

37 T. Jimbo, Y. Sakuma, N. Urakami, P. Ziherl and M. Imai, *Biophys. J.*, 2016, **110**, 1551–1562.

38 S. Svetina and B. Žekš, *Anat. Rec.*, 2002, **268**, 215–225.

39 J. Majhenc, B. Božič, S. Svetina and B. Žekš, *Biochim. Biophys. Acta*, 2004, **1664**, 257–266.

40 R. Lipowsky and H.-G. Döbereiner, *EPL*, 1998, **43**, 219.

41 B. Różycki and R. Lipowsky, *J. Chem. Phys.*, 2016, **145**, 074117.

42 T. Bhatia, S. Christ, J. Steinkühler, R. Dimova and R. Lipowsky, *Soft Matter*, 2020, **16**, 1246–1258.

43 W. Rawicz, K. C. Olbrich, T. McIntosh, D. Needham and E. Evans, *Biophys. J.*, 2000, **79**, 328–339.

44 G. Bolognesi, M. S. Friddin, A. Salehi-Reyhani, N. E. Barlow, N. J. Brooks, O. Ces and Y. Elani, *Nat. Commun.*, 2018, **9**, 1882.

45 N. Yandrapalli and T. Robinson, *Lab Chip*, 2019, **19**, 626–633.

46 B. Kavčič, A. Sakashita, H. Noguchi and P. Ziherl, *Soft Matter*, 2019, **15**, 602–614.